Supramolecular Networks Obtained by Block Copolymer Self-Assembly in a Polymer Matrix: Crystallization Behavior and Its Effect on the Mechanical Response

Ruth N. Schmarsow, Ulises Casado, Marcelo Ceolín, Ileana A. Zucchi, Alejandro J. Müller,* and Walter F. Schroeder*

Read Online

ACCESS | Metrics & More | Article Recommendations | SI Supporting Information

ABSTRACT: In recent years, there has been growing interest in the study of supramolecular networks obtained by self-assembly of amphiphilic molecules due to their responsive behavior to different external stimuli. The possibility of embedding supramolecular networks into polymer matrices opens access to a new generation of functional polymers with great potential for various applications. However, very little is known about how the dynamics of the supramolecular network is affected by diffusional and topological limitations imposed by the polymer matrix. In this work, we investigate the behavior of supramolecular networks embedded into a rubbery polymer. Crystallization-driven self-assembly of a poly(ethylene-*block*-ethylene oxide) (PE-*b*-PEO) diblock copolymer was used to generate supramolecular networks in dimethacrylate monomers, which were then photopolymerized at room temperature. PE-*b*-PEO self-assembles into nanoribbons with a semicrystalline PE core bordered by coronal chains of PEO, and the nanoribbons, in turn, bundle into lamellar aggregates with an average stacking period of around 45 nm. The nanoribbons are interconnected through crystalline nodes in a 3D network structure. Small-angle X-ray scattering experiments show that the polymer matrix preserves the structure of the supramolecular network and avoids its disintegration when the material is heated above the melting temperature of PE cores. Successive self-nucleation and annealing studies reveal that the polymer matrix does not influence the crystallization−melting processes of PE, which take place through the interconnected cores of the supramolecular network. In contrast, the matrix imposes strong effects of topological confinement on the crystallization of PEO, limiting the dimensions of the crystalline lamellae that can be formed. Mechanical tests show that the deformation capacity of these materials can be precisely tuned by programming the temperature within the melting range of the supramolecular network. This behavior was also characterized by shape memory cyclic tests.
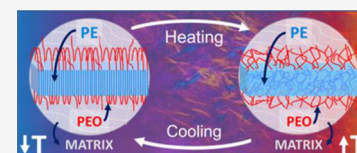
INTRODUCTION

The study of supramolecular networks has been attracting growing interest in the last decade due to the ability of this type of structure to respond to different external stimuli.[1−3] This feature gives them enormous potential for the design of new and sophisticated functional materials. Supramolecular gels are obtained from amphiphilic molecules (so-called gelators) that self-assemble in a suitable solvent forming elongated structures, such as fibers, strands, or ribbons. These structures are connected by non-covalent interactions (e.g., van der Waals, hydrogen bonds, $\pi-\pi$ stacking, crystallization, or charge transfer), generating 3D networks that encapsulate the solvent and prevent its flow.[4] Due to the dynamic and reversible nature of the non-covalent interactions, these supramolecular gels have the ability to respond to external stimuli, such as light, temperature, ultrasound, pH, and redox changes.[5−9] The most attractive feature of these materials is the possibility of precisely controlling the morphology and properties of the network through the chemical structure of the gelator. In this way, it is possible to access a wide variety of functional materials for applications in separation, sensing,

optoelectronics, self-healing, and shape memory technologies, among others.[10]

Elongated nanostructures, capable of forming 3D networks, can be prepared by self-assembly of block copolymers (BCPs) in selective solvents.[11−15] With this method, it is possible to obtain a variety of micellar structures, including spheres, cylinders, vesicles, ribbons, and other more complex shapes. In the self-assembly process, the micellar structure is determined by an interplay between different factors, such as molar mass, block ratio, concentration, and temperature, among others.[16,17] If the core-forming block can crystallize, self-assembly follows an epitaxial growth process that generates structures with a low surface curvature. This approach, termed crystallization-driven self-assembly (CDSA), commonly leads to elongated micelles,
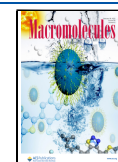
such as fibers and ribbons. Recently, Manners' group used a B-A-B triblock copolymer with crystallizable B segments to obtain fiber-like micelle networks.[18] It was found that the copolymer concentration and the addition of a common solvent fraction were critical variables in achieving macroscopic gels.

The possibility of embedding supramolecular networks into polymer matrices opens access to a new generation of functional materials with a wide range of applications. These materials can be prepared through a two-step protocol. First, gelator molecules are self-assembled in a reactive monomer to produce a supramolecular network. Under these conditions, the monomer will remain encapsulated in the 3D network below the sol−gel transition temperature. Then, low-temperature photopolymerization is used to generate the polymer matrix preserving the structural features of the supramolecular network. In this way, it is possible to develop advanced materials that synergistically combine the responsive, tunable, and programmable nature of the supramolecular network with the mechanical strength provided by the polymer matrix.

There are relatively few studies reported so far on supramolecular networks embedded into polymer matrices. The first example was from Möller and co-workers.[19] They used two different compounds [i.e., (perfluoroalkyl) alkanes and benzo-15-crown-5 benzoate] as organic gelators of methacrylate monomers, which were subsequently UV-photocured to obtain reversible networks embedded into crosslinked polymer matrices. Supramolecular networks were leached to obtain nanoporous membranes, which were then functionalized by charging the pore walls with ionic sites. Also, supramolecular networks have been embedded into polymer matrices to obtain materials with improved mechanical properties.

Stupp and co-workers prepared gel-forming nanoribbons by self-assembling dendron rod-coil molecules in a styrene monomer.[20] After matrix polymerization, the resulting materials exhibited enhanced chain orientation and significantly improved impact strength. As demonstrated, the nanoribbon network increased the alignment of polystyrene chains, limiting crack propagation, and also acted as a nano-skeleton that dissipated impact energy. Furthermore, the network imparted a degree of self-healing to the deforming material, as dynamic non-covalent interactions could reform after breaking under mechanical stress. In other studies, thermal and physical properties have also been enhanced by embedding supramolecular networks into polymer matrices.[21−25]

Currently, very little is known about how the formation−disintegration dynamics of the supramolecular network is affected by diffusional and topological limitations imposed by the polymer matrix. Understanding these effects is crucial to designing materials responsive to external stimuli with well-tuned functionalities. In this work, we investigate the behavior of supramolecular networks obtained by CDSA of a poly-(ethylene-*block*-ethylene oxide) diblock copolymer in a low glass transition temperature dimethacrylate matrix. Supramolecular structures were characterized by small-angle X-ray scattering (SAXS), differential scanning calorimetry (DSC), and oscillatory rheology techniques. Applying self-nucleation (SN) and successive self-nucleation and annealing (SSA) protocols, we were able to describe how the polymer matrix influences the response of the 3D network structure. The

mechanical properties and memory shape effects of these materials were also analyzed.

EXPERIMENTAL SECTION

Materials. Poly(ethylene glycol) dimethacrylate (PEGDMA, M_n = 550) was purchased from Aldrich Chemical Co. The block copolymer used was PE-*b*-PEO (M_n = 1400; 50 wt % PEO, Aldrich Chemical Co.), while camphorquinone (CQ, Aldrich Chemical Co.) was employed as a radical photoinitiator for the visible light polymerization of PEGDMA. The chemical structures of these compounds are shown in Figure 1. All materials were used without previous treatment.
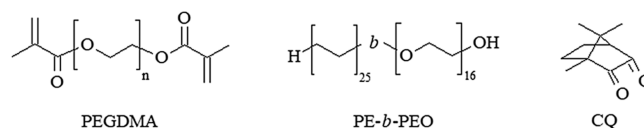

Figure 1. Chemical structure of the used materials.

Sample Preparation. An appropriate amount of PE-*b*-PEO was placed in a glass vial and then one-half of the total mass of PEGDMA was added. To prevent degradation of PEO blocks during blending at high temperature, the mixture was previously purged with nitrogen for 30 min. Then, the mixture was heated to 120 °C and stirred for 5 min to disperse the BCP in PEGDMA. Subsequently, the vial was cooled to room temperature and the remaining mass of PEGDMA with 2 wt % CQ was added. After that, the mixture was again purged with nitrogen for 15 min and then heated to 120 °C and stirred for around 1 min until a homogeneous dispersion was obtained. Immediately afterward, the mixture was cast between two glass covers separated by a 2 mm spacer. The sample was irradiated at 25 °C using an array of blue LEDs with λ in the range of 410−530 nm and I = 60 mW/cm^2 (OptoTech, Germany).

Characterization Techniques. *Fourier Transform Infrared Spectroscopy.* Conversion of methacrylate double bonds was measured by near-infrared spectroscopy using a Nicolet 6700 Thermo Scientific device. Measurements were performed in transmission mode, in the range of 4000−7000 cm^{-1}, with a resolution of 4 cm^{-1}. A drop of the sample was sandwiched between two glass plates separated by a 2 mm spacer used to regulate the sample thickness. Specimens were irradiated in situ at 25 °C, and spectra were collected at regular time intervals. Conversion profiles were calculated from the decay of the methacrylate peak at 6165 cm^{-1} (first overtone of the group = CH$_2$), without previous normalization.

Differential Scanning Calorimetry. Samples were analyzed with a PerkinElmer Pyris 1 instrument equipped with a cooling accessory (Intracooler 2, PerkinElmer), using dry nitrogen as purge gas. For non-isothermal tests, a sample mass of ∼5 mg was placed in an aluminum pan and analyzed by heating and cooling cycles. First, the sample was heated up to 120 °C (first heating scan) and kept isothermally for 3 min to erase all crystalline memory. Subsequently, the sample was cooled down to −60 °C (cooling scan) and finally heated from −60 to 120 °C (second heating scan). All the scans were performed at 20 °C/min.

The isothermal crystallization kinetics of PE was measured by a step procedure, employing the following protocol:[26,27] (i) heating to 120 °C for 3 min to erase any previous crystalline state; (ii) fast cooling (at 60 °C/min) from 120 °C to the isothermal crystallization temperature (T_c); (iii) keeping at T_c for a crystallization time (t_c); (iv) heating at 20 °C/min from T_c to 120 °C, where the crystalline fraction developed during step iii is determined by quantifying the melting enthalpy; (v) steps i−iv are repeated employing the same T_c but with increasing values of t_c, until the melting enthalpy remains constant. The whole process was repeated for different values of T_c.

SN experiments were carried out following the method first proposed by Fillon et al.[28] and extensively used by Müller and co-workers[29,30] through the following protocol: (i) heating to 120 °C for
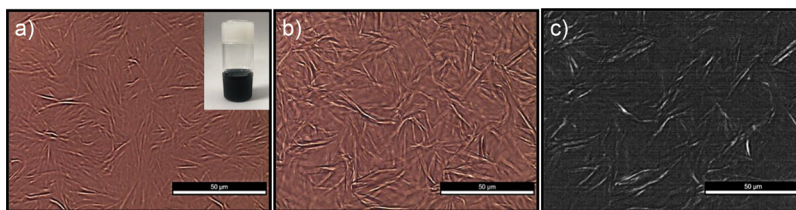
Figure 2. Optical microscopy of PE-*b*-PEO/PEGDMA blends at room temperature: (a) and (b) correspond to TOM images of samples containing 10 and 30 wt % BCP, respectively; while (c) corresponds to a PLOM image of the sample with 30 wt % BCP. In each image, the white bar represents 50 μm. The inset in (a) shows a digital image of the inverted vial containing the gel formed with 10 wt % BCP.

3 min to erase all crystalline memory; (ii) cooling down to 25 °C at 20 °C/min, to create a standard thermal history; (iii) heating at 10 °C/min up to an *self-nucleation temperature* (T_s) and keeping at this T_s for 5 min; (iv) cooling from T_s to room temperature at 20 °C/min, where changes in crystallization due to SN are recorded; (v) final heating from room temperature to 120 °C at 20 °C/min, in order to reveal changes in the melting behavior due to the thermal treatment.

SSA analysis was performed according to the protocol originally developed by Müller et al.[31−33] The first part of this experiment consists of the same steps i−iii of the SN method (described above), using $T_{s,ideal}$ as the self-nucleation temperature in step iii. Then, the following steps are performed: (iv) cooling from $T_{s,ideal}$ to room temperature at 20 °C/min, where the molten fraction crystallizes using the unmolten crystal fragments or melt memory as self-nuclei; (v) heating at 20 °C/min from room temperature to a new T_s, which is 5 °C lower than the previous one, and keeping at this T_s for 5 min, where unmolten crystals undergo annealing and some molten species can isothermally crystallize; (vi) cooling from T_s to room temperature at 20 °C/min, where the rest of the molten species crystallize; (vii) steps v and vi are repeated over the entire melting range of the sample; (viii) final heating from room temperature to 120 °C at 20 °C/min, where the effect of the SSA treatment is revealed through the melting behavior.

Small-Angle X-ray Scattering. A XEUSS 1.0 HR (XENOCS, Grenoble) apparatus with a Pilatus 100 K detector (Dectris, Switzerland) and a microfocus X-ray source (λ = 1.5419 Å) was used. The sample was placed at 1354 mm from the detector, and spectra were collected with an acquisition time of 3 min. A HFSX350 device (Linkam Scientific Instruments) was used to control the sample temperature. To obtain 1D-SAXS curves, circular integration of the 2D data was performed using standard procedures. Scattering curves were analyzed with the SASfit software package.[34]

Optical Microscopy. Transmission optical microscopy (TOM) images were taken with a Leica DC 100 camera on a Leica DMLB microscope. A sample drop between glass plates was placed on a hot stage (Linkam TMS 93) to acquire images at several temperatures. Polarized light optical microscopy (PLOM) observations were performed by placing the sample between two crossed polarizers.

Rheometry. To characterize the rheological behavior of the systems before photocuring, changes in the storage (G') and loss (G'') moduli with temperature were followed using an Anton Paar rheometer (model Physica MCR-301, with a CTD 600 thermochamber). Measurements were performed using a parallel-plate configuration (25 mm diameter and 1 mm gap) in an oscillatory mode, setting an amplitude of 0.1% at a frequency of 1 Hz. For measurements of viscosity as a function of temperature, a setup of 10 rpm was used with the same geometric parameters.

Mechanical Properties. Stress−strain curves of photocured samples were acquired using a Perkin-Elmer DMA 7e, under controlled force mode. Rectangular specimens of 15 × 5 × 1 mm were tested using a three-point bending geometry with a span of 10 mm and an applied initial stress of 10 mN. Measurements were performed at 30 and 80 °C under a nitrogen atmosphere.

On the other hand, changes in the storage modulus (G') as a function of temperature were recorded with an Anton Paar rheometer (model Physica MCR-301, with a CTD 600 thermochamber). Rectangular specimens of 20 × 5 × 1 mm were measured using a

torsion geometry at a frequency of 1 Hz and an applied deformation of 0.05%. The temperature range was from −60 to 120 °C at 5 °C/min.

Shape Memory Behavior. Strain-recovery cyclic tests were performed using an Anton Paar rheometer (model Physica MCR 301, with a CTD 600 thermochamber). Rectangular specimens of 20 × 5 × 1 mm were measured employing a torsion geometry, under controlled force mode. The following thermomechanical cycles were applied: (1) The sample with an original strain $[\varepsilon_p(N − 1)]$ was heated to T_{high} (30 or 80 °C) at 5 °C/min and kept at T_{high} for 10 min. (2) Then, a linear stress ramp from 0 to 0.6 MPa was applied at a constant temperature. (3) The sample was then cooled from T_{high} to −35 °C at 5 °C/min, under constant stress. (4) Temperature and stress conditions were kept constant for 60 min, where a maximum deformed strain ($\varepsilon_d(N)$) was achieved. (5) Then, stress was linearly removed from 0.6 to 0 MPa at constant temperature. (5) Conditions were kept constant for 30 min, obtaining the so-called fixed strain ($\varepsilon_f(N)$). (6) The sample was subsequently heated from −35 to T_{high} at 5 °C/min under constant stress. (7) Conditions were kept constant for 60 min, where a residual strain ($\varepsilon_p(N)$) was recorded. (8) Steps 2−7 were repeated until four cycles in total were completed. For each cycle (N), it was possible to calculate the shape fixity ratio (R_f) and shape recovery ratio (R_r):

$$R_f = \frac{\varepsilon_f(N) - \varepsilon_p(N-1)}{\varepsilon_d(N) - \varepsilon_p(N-1)} \times 100 \tag{1}$$

$$R_r = \frac{\varepsilon_f(N) - \varepsilon_p(N)}{\varepsilon_f(N) - \varepsilon_p(N-1)} \times 100 \tag{2}$$

■ RESULTS AND DISCUSSION

Supramolecular gels were obtained by self-assembly of a PE-*b*-PEO diblock copolymer in PEGDMA monomer, which is a selective solvent for the PEO block. For the self-assembly process, the BCP was first dispersed in PEGDMA at 120 °C, where PE and PEO blocks are in the molten state. Once a homogeneous dispersion was obtained, the blend was allowed to cool to room temperature. During cooling, the appearance of the sample changed from transparent to cloudy, denoting the formation of elongated micellar structures driven by PE crystallization. Immediately afterward, gelation took place due to the formation of a micellar network. The gelation process was followed by optical microscopy in real time, as shown in Video S1 and Figure S1.

Figure 2a,b shows TOM images at room temperature of blends containing 10 and 30 wt % PE-*b*-PEO in a PEGDMA monomer. Both samples exhibit micellar aggregates several micrometers long, which are interconnected, forming a supramolecular network structure. Gelation was visually evidenced by the immobilization of the dimethacrylate monomer and the absence of flow when the vial containing the sample was inverted (inset in Figure 2a). Figure 2c shows a PLOM image of the blend containing 30 wt % PE-*b*-PEO at
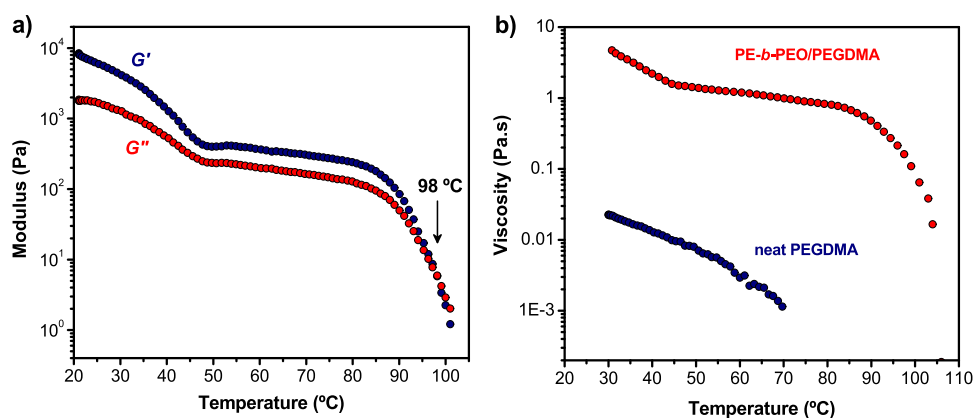
Figure 3. (a) Storage (G') and loss (G'') moduli as a function of temperature for the blend containing 10 wt % PE-*b*-PEO in PEGDMA and (b) evolution of viscosity with temperature for both the blend with 10 wt % PE-*b*-PEO and the neat monomer.
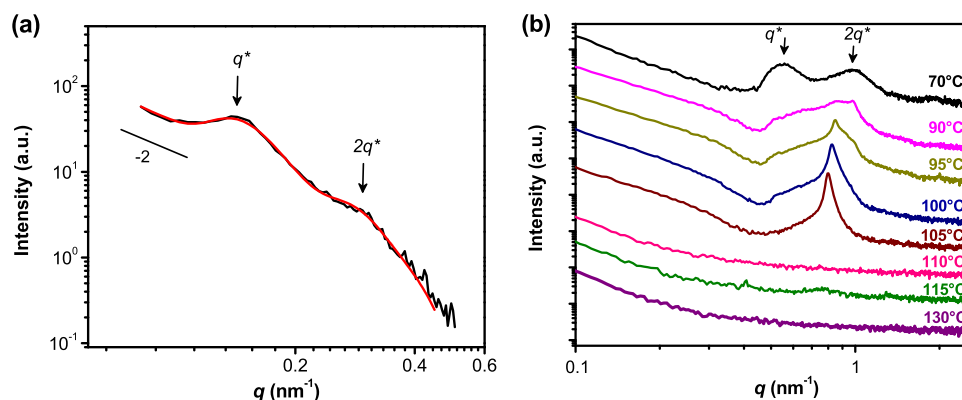

Figure 4. SAXS data for (a) photocured sample containing 10 wt % PE-*b*-PEO in PEGDMA at 25 °C. The black line represents the experimental data, and the red line is the fitting curve using a model of elongated planar objects (homogeneous XS algorithm) with a lamellar structure factor (paracrystalline model). (b) Neat PE-*b*-PEO block copolymer at different temperatures (reproduced from ref 36. with permission from the Royal Society of Chemistry).

room temperature, where the crystalline nature of the micellar cores is revealed. Similar characteristics were obtained for samples with 10 and 20 wt % BCP (Figure S2).

Supramolecular gels were characterized by oscillatory rheology. Figure 3a shows the storage (G') and loss (G'') moduli as a function of temperature for the blend containing 10 wt % PE-*b*-PEO in PEGDMA monomer. Below 98 °C, G' values are larger than G'' values, implying that the sample exhibits a gel behavior. At 98 °C, a crossover of both moduli occurs, indicating a transition from gel to liquid, produced by the disintegration of the supramolecular network in the PEGDMA monomer. The crossover temperature agrees with the melting peak of PE blocks, as shown in Figure S3. These results indicate that PE crystals play a crucial role in providing structural integrity to these supramolecular networks. The drop in G' and G'' values around 40 °C is attributed to the melting of PEO crystals, as discussed below.

Figure 3b shows the evolution of viscosity with temperature for both the blend with 10 wt % PE-*b*-PEO and the neat monomer. At 30 °C, the viscosity value of the blend in the gel state (4.68 Pa.s) is two orders of magnitude higher than that of the neat monomer (0.023 Pa.s). As can be seen, the viscosity of the blend significantly decreases around 40 °C due to the melting of PEO crystals and then drops dramatically above 90 °C due to the melting of PE crystals, reaching, at 104 °C, the same viscosity value as that of the neat monomer at 30 °C.

The obtained gels were irradiated at room temperature to photopolymerize the PEGDMA monomer. FTIR spectroscopy was used to monitor the polymerization reaction by measuring the decay of the methacrylate peak at 6165 cm^{-1}. All samples underwent efficient polymerization, resulting in methacrylate conversions greater than 90% after 5 min irradiation (see Figure S4). In this way, supramolecular networks were embedded in a crosslinked dimethacrylate matrix, which is in a rubbery state at room temperature, as will be discussed later.

Photocured materials were analyzed by SAXS to investigate the nanoscale structure of the micellar network. As an example, the scattering profile recorded for the sample with 10 wt % PE-*b*-PEO at room temperature is shown in Figure 4a. At low *q*-values, the scattering curve exhibits a slope of −2 that is characteristic of planar nanostructures.[35] These structures are spatially correlated, as indicated by the presence of a main maximum at $q^* = 0.14$ nm^{-1} and a secondary maximum at $2q^*$. This sequence corresponds to a lamellar structure of elongated planar nanoobjects with an average lamellar period of 44.9 nm ($2\pi/q^*$). Based on this evidence, we analyzed SAXS data using the SASfit software package.[34] The scattering curve was modeled using a form factor for elongated planar objects (homogeneous XS model) and a lamellar structure factor (paracrystalline model). Fitting to SAXS data led to a thickness for planar objects of 10.7 nm with an average stacking distance of 40.5 nm. The best-fitting parameters are presented in Table S1. With these values, an excellent fitting was obtained, as
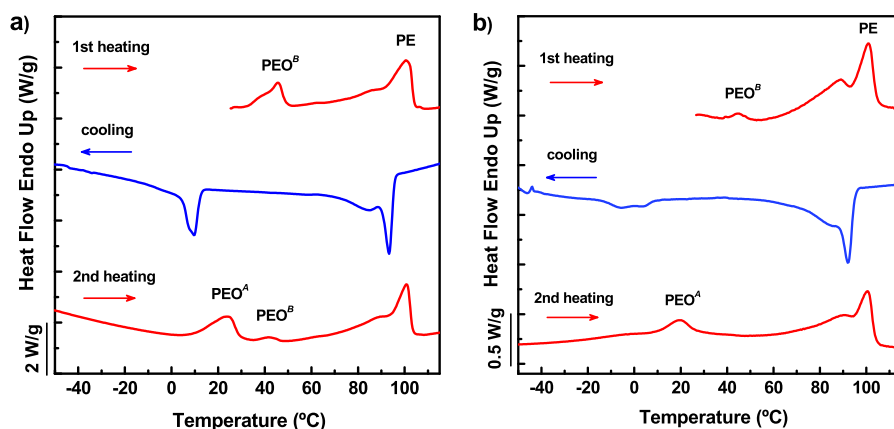
Figure 5. DSC scans at 20 °C/min for: (a) neat PE-*b*-PEO block copolymer and (b) photocured 30 wt % PE-*b*-PEO/PEGDMA blend. PEO^A corresponds to crystals comprised of once-folded chains, while PEO^B corresponds to crystals with fully extended chains.

shown in Figure 4a. Based on these results, we can infer that the gel structure consists of lamellar aggregates of nanoribbons that are interconnected forming a supramolecular network. In turn, nanoribbons are formed by a semicrystalline PE core bordered by coronal chains of PEO.

Analysis of the Crystallization Process. DSC measurements were performed on nanostructured materials obtained after photopolymerization. For reference, we first analyzed the neat PE-*b*-PEO block copolymer, which presents a lamellar morphology at room temperature with the order−disorder transition located at 110 °C (see Figure 4b). Figure 5a shows heating and cooling DSC scans for the neat BCP. The first heating scan displays an endotherm at 46 °C assigned to the melting of PEO crystals, followed by a broad endotherm with a main peak at 101 °C due to the melting of PE crystals. This is the typical melting behavior of PE blocks obtained by hydrogenation of polybutadiene, where ethyl branches generated by 1,2-addition define a distribution of methylene linear sequences that crystallize and melt depending on their length, which means that the lower the melting and crystallization temperatures, the shorter the sequence.[37]

Following the first heating scan (Figure 5a), the cooling cycle shows an exothermic peak at 94 °C, characteristic of the crystallization of PE blocks in an unconfined lamellar phase, and another peak at 10 °C assigned to the confined crystallization of PEO blocks between crystalline PE lamellae. Within a confined space, the crystallization of PEO is hindered. In fact, the second heating scan shows two distinct melting peaks for PEO blocks, attributed to the co-existence of crystalline lamellae with different chain conformations. The endotherm at 25 °C (labeled as *A*) is assigned to crystals comprised of once-folded chains, while the endotherm at 42 °C (labeled as *B*) is due to crystals comprised of fully extended chains. This assignment is supported by the observation that low molar mass PEO oligomers (with chain lengths even shorter than the PEO block in the present study) are able to form crystalline lamellae not only with extended chains, but also with once-folded chains.[38] It has been well established that the chain folding has a direct influence on the melting temperature of the crystal lamella, according to the Gibbs−Thomson equation,[39] which is expressed as:

$$T_m = T_m^\infty \left(1 - \frac{2\gamma V_c}{L \Delta H_m}\right) \qquad (3)$$

where T_m^∞ is the equilibrium melting temperature of an infinitely large crystal, γ is the interfacial tension between the crystalline phase and the amorphous phase, V_c is the molar volume of a crystallizable repeat unit, L is the lamellar thickness, and ΔH_m is the enthalpy of melting (per mole of crystalline units) of a 100% crystalline polymer. PEO crystallizes in a 7_2 helical structure with a pitch of ∼1.95 nm.[40] Therefore, the theoretical thickness of a lamella containing n-folded chains is given by $L = \frac{1}{n+1}\frac{1.95}{7}N$, where N is the degree of polymerization of PEO.

We applied the Gibbs−Thomson equation to the PEO block of the copolymer used in this study, with $T_m^\infty = 68.9$ °C (341.9 K), $\gamma = 37.9$ mJ/m², $V_c = 36.6$ cm³/mol, and $\Delta H_m = 8650$ J/mol.[41−43] From the calculations, the estimated melting temperatures for crystals with once-folded chains ($n = 1$) and fully extended chains ($n = 0$) were 20 and 44 °C, respectively, which are consistent with the assignment of the endotherms labeled *A* and *B* in the heating DSC scans. Regarding the melting behavior of PE blocks in Figure 5a, it was practically the same as in the first heating scan.

Figure 5b shows DSC scans for the photocured material containing 30 wt % PE-*b*-PEO in PEGDMA. Several remarks emerge from the inspection of the curves obtained. The first observation is that PE blocks in the micellar core exhibit similar behavior to that shown in the neat block copolymer (see Figure 5a). This result is consistent with the presence of elongated micellar nanostructures, where PE crystal growth can reach micrometer dimensions in an unconfined environment. It should be noted that for the photocured sample with 5 wt % PE-*b*-PEO, the crystallization peak of PE was slightly shifted toward a lower temperature, indicating a small degree of confinement (Figure S5). A second observation in Figure 5b is that PEO chains in the micellar corona are able to crystallize. As can be seen, the first heating scan shows a melting peak at 44 °C associated to PEO crystals with a conformation of fully extended chains (endotherm "B"). These crystals were formed in the PEGDMA monomer, prior to the photopolymerization reaction, as discussed in Figure 3. Note that during the DSC cooling scan, crystallization conditions of PEO are markedly different. Here, topological confinement effects imposed by the crosslinked dimethacrylate matrix limit the size of the crystalline lamellae that can be formed, which exclusively adopt the conformation of once-folded chains. This is evidenced in the subsequent heating scan, where all the

crystalized PEO melted in the endotherm "A." Similar characteristics were obtained for materials containing 20, 10, and 5 wt % PE-*b*-PEO, as shown in Figure S5.

We also analyzed whether the supramolecular network embedded in the crosslinked dimethacrylate matrix disintegrates when the material is heating at 120 °C, above the melting temperature of PE. SAXS profiles recorded at 60 and 120 °C for the sample with 10 wt % PE-*b*-PEO are shown in Figure 6. Both curves are similar and can be satisfactorily fitted
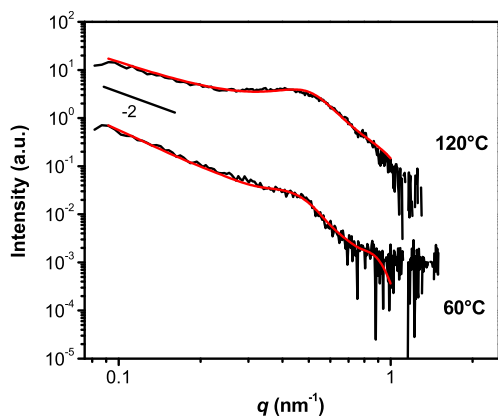

Figure 6. SAXS data at 60 and 120 °C for the photocured sample containing 10 wt % PE-*b*-PEO. The black lines represent the experimental data, and the red lines are the fitting curves using a model of elongated planar objects (homogeneous XS algorithm) with a lamellar structure factor.

using the same form factor as in Figure 4a (Homogeneous XS), with different structure factors: Paracrystalline model for 60 °C and Hard Sphere Repulsion Radius model for 120 °C (best-fitting parameters are shown in Table S2). It should be noted that the broadening of the SAXS peak at 120 °C could be associated with the thermal disorder of the spatially correlated phases when going from a semicrystalline state (at 60 °C) to a molten state (at 120 °C). According to these results, we can infer that the crosslinked matrix preserves the structure of the supramolecular network and avoids its disintegration when the material is heated above the melting temperature of PE cores. This idea was also supported by optical microscopy (Figure S6). When a photopolymerized sample was analyzed by

PLOM applying repeated cycles of heating and cooling, we observed that the crystalline domains always appeared in exactly the same positions. However, when the same protocol was repeated for a non-photopolymerized blend, the topology of the crystalline network changed in each cooling cycle.

A very important aspect that needs to be explored is the type of junctions (nodes) that keep the ribbon-like micelles connected since they provide rigidity to the supramolecular network. With this idea in mind and using an isothermal step crystallization protocol, we analyzed the crystallization kinetics of PE.[26,27] Figure 7a shows the relative crystallinity of PE as a function of time for a temperature of 100 °C. In this figure, relative crystallinity values were calculated considering complete crystallization when the crystallization exotherm returned to baseline. As can be seen, all the curves presented a sigmoidal shape, according to the conventional crystallization mechanism where PE crystal growth propagates over a long range from heterogeneous nuclei.

The data corresponding to the beginning of PE crystallization (i.e., for values between 0.05 and 0.35 of relative crystallinity) were fitted to the linearized form of the Avrami equation:[44,45]

$$\log[-\ln(1 - V_c(t - t_0))] = \log(k) + n\log(t - t_0) \qquad (4)$$

where V_c is the crystalline volumetric fraction developed at time t, t_0 is the induction time, k is an overall rate constant for nucleation and growth, and n is a constant known as the Avrami index. Eq 4 is derived from first principles, and hence, the Avrami index has physical significance. As proposed by Michell and Müller,[46] two contributions can be considered within the value of n, one due to primary nucleation (instantaneous = 0, sporadic = 1), and another due to the growth dimensionality [one-dimensional crystals =1, axialites (2D) = 2, spherulites (3D) = 3]. For all samples analyzed, the calculated Avrami indices ranged around 1.6–1.8 (Figure S7). Within experimental errors, these values are consistent with 2D crystal aggregates instantaneously nucleated, which is in agreement with the formation of lamellar arrangements due to the tendency of ribbon-like micelles to adopt face-to-face packing, as discussed above.

Figure 7b shows the relative crystallization rate of PE blocks (expressed as the inverse of the half-crystallization time, $1/\tau_{50\%}$) as a function of the crystallization temperature. As can be
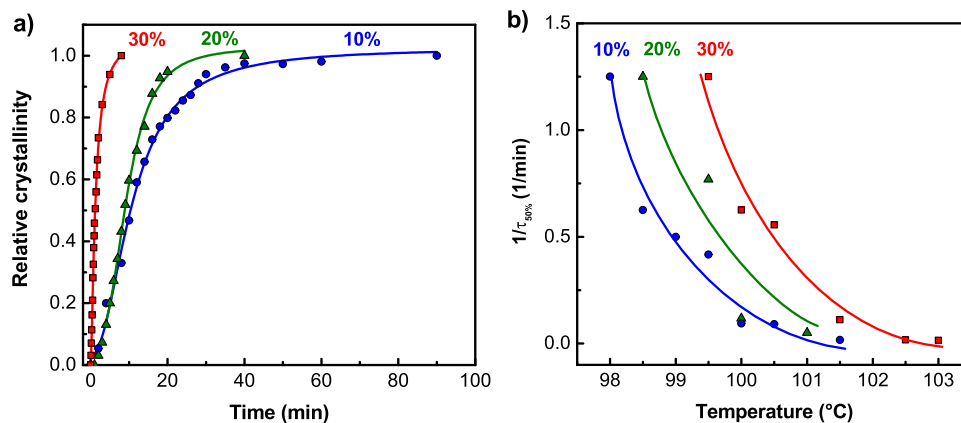

Figure 7. Isothermal step crystallization of PE blocks in photocured samples containing different amounts of BCP (10, 20, and 30 wt %) in PEGDMA. (a) Development of relative crystallinity with time at a temperature of 100 °C (lines represent the fitting of data to sigmoidal functions). (b) Inverse of crystallization half-time as a function of crystallization temperature (lines were drawn to guide the eye).

seen, the curves show a trend of reduction in the crystallization rate with temperature, due to the decrease in supercooling. For a given temperature, the relative crystallization rate increases with the amount of BCP in the dimethacrylate matrix (Figure 7b). Taking into account that crystal growth probably dominates the overall crystallization kinetics (since nucleation of PE is heterogeneous and instantaneous), the obtained result is consistent with an increase in the degree of percolation of PE cores and allows us to infer that ribbon-like micelles are interconnected through crystalline nodes. We speculate that these nodes were generated by branching processes due to crystallographic mismatch,[47] which took place during epitaxial growth of ribbon-like micelles in the PEGDMA monomer. Figure 8 shows a schematic illustration of the structure of the
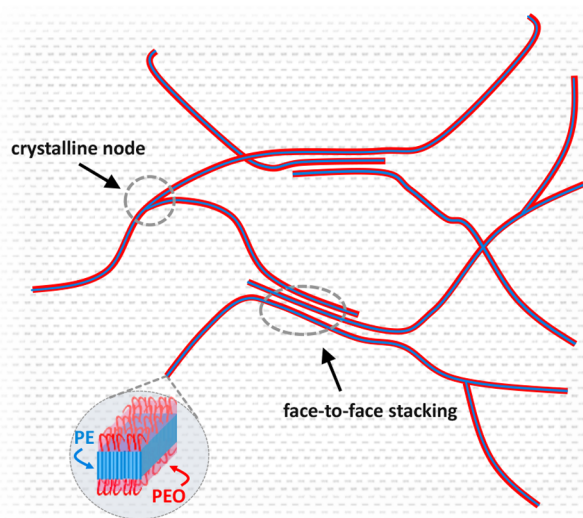

Figure 8. Schematic illustration of the structure of the supramolecular network.

supramolecular network indicating the two different types of junctions that keep the ribbon-like micelles connected, that is, crystalline nodes and face-to-face stacking.

For a deeper insight into the crystal structure of supra-molecular networks, we employed SN and SSA techniques, following the protocols detailed in the Experimental Section.

Cooling and subsequent heating scans after SN treatment at the indicated self-nucleation temperature (T_s) are shown in Figure 9a,b, respectively, for the sample with 30 wt % BCP. Note that in these SN experiments, only the crystallization behavior of PE is analyzed. Three different self-nucleation domains can be distinguished depending on the applied T_s. Complete melting domain or *Domain I* (red lines) was characterized by a constant crystallization temperature (T_c = 92.8 °C) upon cooling from T_s. It was detected at sufficiently high T_s values, where all crystalline memory was erased, and no self-nuclei could survive. Self-nucleation domain or *Domain II* (blue lines) took place at intermediate T_s values, where some self-nuclei were produced and were capable of increasing the nucleation density during subsequent cooling from T_s. In this domain, T_c shifts toward higher temperatures as T_s decreases. Finally, self-nucleation and annealing domain or *Domain III* (green lines) was observed at lower T_s values, where melting was incomplete. In this case, the remaining crystals underwent annealing during the time at T_s, while the molten fraction was self-nucleated through cooling from T_s. This domain was
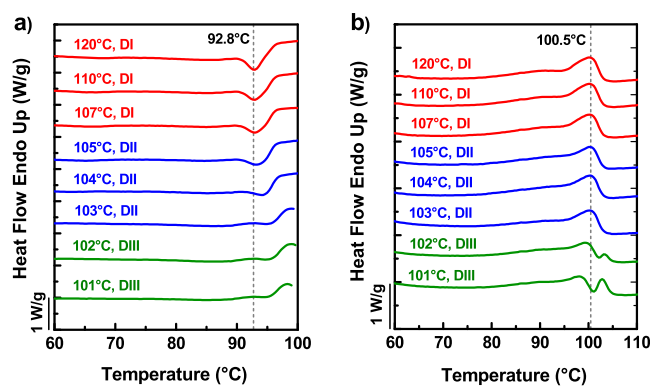

Figure 9. Cooling (a) and heating (b) DSC scans after SN at different T_s values (as indicated above each curve) for a photocured sample containing 30 wt % PE-*b*-PEO.

characterized by the appearance of a second melting peak in the following heating scan. Similar results were obtained for photocured specimens containing 20, 10, and 5 wt % PE-*b*-PEO (Figures S8−S10, respectively).

The lowest T_s value within *Domain II* (103 °C) is defined as the *ideal self-nucleation temperature* ($T_{s,ideal}$), where there is maximum SN without annealing. This $T_{s,ideal}$ value was used as the first self-nucleation temperature in the SSA protocol. The final heating DSC scans subsequent to SSA thermal treatment for neat BCP and photocured BCP/PEGDMA samples containing different amounts of BCP are shown in Figure 10.
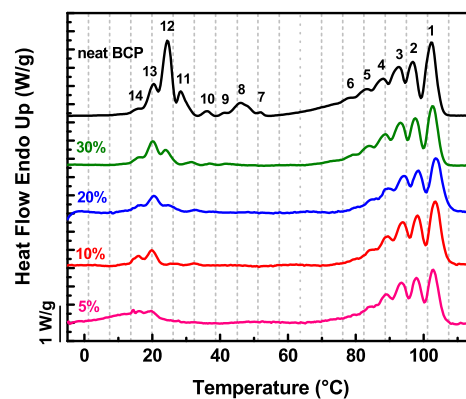

Figure 10. DSC heating scans after the SSA thermal treatment for neat BCP and photocured BCP/PEGDMA samples with different amounts of BCP. The curves were normalized in function to the PE content.

As can be seen, fractionated PE exhibited six endothermic peaks as a result of the melting of crystalline fractions with diverse lamellar thickness. All photocured samples showed the same PE fractionation pattern as neat BCP. These results show that the crosslinked dimethacrylate matrix does not signifi-cantly influence the crystallization process of PE, which takes place through the interconnected cores of the supramolecular network. This is consistent with our previous evidence.

Figure 10 also shows the fractionation of the PEO component. Fractions number 7, 8, 9, and 10 in neat BCP correspond to PEO lamellae with nearly fully extended chain conformation (endotherm *B* in Figure 5). These fractions are present in the photocured BCP/PEGDMA samples in very low percentages due to the inability of PEO chains to adopt this conformation in the crosslinked matrix. As can be seen,
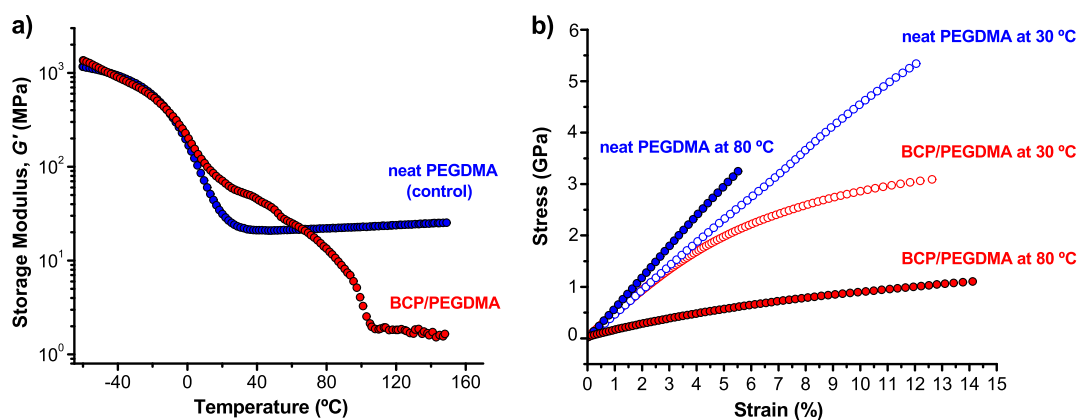
Figure 11. Mechanical behavior of the photocured material with 10 wt % BCP using the neat PEGDMA matrix as a control. (a) Storage modulus (G') vs temperature and (b) stress−strain curves at 30 and 80 °C.

fractions number 11, 12, 13, and 14, which correspond to PEO lamellae with once-folded chains (endotherm *A* in Figure 5) show a different distribution in the photocured samples than in neat BCP. The largest fraction in neat BCP (number 12) is found at a higher temperature and therefore corresponds to thicker lamellae (formed by longer crystallizable sequence lengths) than the largest fraction in the photocured samples (number 13). This is owing to the greater difficulties experienced by the PEO chains to fold and crystallize in the crosslinked matrix with respect to neat BCP. These results show that the matrix imposes strong effects of topological confinement on the crystallization of PEO, limiting the dimensions of the crystalline lamellae that can be formed.

Mechanical Characterization and Shape Memory Effect. To analyze how the supramolecular network influences the mechanical behavior of the material, we tested a sample with 10 wt % PE-*b*-PEO. As a control dimethacrylate network, we used a neat PEGDMA sample photopolymerized under the same conditions as the BCP/PEGDMA materials. Figure 11a shows the changes in storage modulus (G') as a function of temperature. Both samples exhibit a marked decrease in G'' around −15 °C (onset value) assigned to the T_g of the dimethacrylate matrix. At higher temperatures, the modulus of the BCP/PEGDMA material is higher than that of neat PEGDMA up to 70 °C, where a crossover is observed due to the start of PE melting. Note that the BCP/PEGDMA material presents a small drop in G' around 40 °C due to the melting of PEO blocks. Based on these results, we chose 30 and 80 °C as two specific temperatures (on both sides of the crossover point) to analyze the effect of the partial melting of the supramolecular network. Figure 11b shows stress−strain curves recorded at both temperatures. As can be seen, the greatest differences in mechanical response were obtained at 80 °C, where the BCP/PEGDMA material exhibits a significant increase in ultimate strain as compared to the neat matrix. This softening effect results from a marked decrease in elastic modulus due to partial melting of the supramolecular network.

The results obtained led us to explore the shape memory properties of these materials. Figure 12a,b show strain-recovery tests under controlled force mode, for the BCP/PEGDMA material and the neat matrix, respectively. For these experiments, four thermomechanical cycles were performed setting 80 °C as the high temperature (T_{high}) and −35 °C as the low temperature (T_{low}), where the temporary shape is fixed. Note that T_{low} is below the T_g of the dimethacrylate matrix. As seen
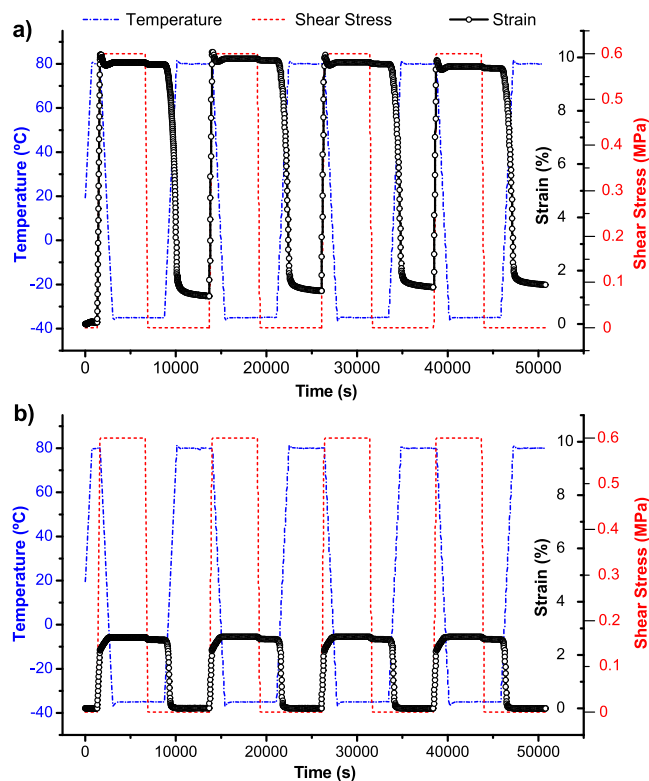

Figure 12. Strain recovery cyclic tests under controlled force mode setting T_{high} = 80 °C and T_{low} = −35 °C for (a) BCP/PEGDMA and (b) neat PEGDMA.

in Figure 12a, there is a strain hysteresis in the first cycle and almost no difference from the second to the fourth cycle. The hysteresis effect in the first cycle has been attributed to irreversible strain generated by residual stress from processing.[48] The resulting values from cycles 2−4 of shape fixity ratio (R_f) and shape recovery ratio (R_r) are listed in Table 1. Both samples exhibited repeatable cycling performance with high

Table 1. Shape Fixity (R_f) and Shape Recovery (R_r) Ratios Calculated from Cycles 2−4

	R_f (%)	R_r (%)
BCP/PEGDMA	99.2 ± 0.1	98.3 ± 0.6
neat PEGDMA	96.5 ± 0.2	99.9 ± 0.1

ability to fix a temporary shape and recover its original shape. However, the maximum deformed strain for the BCP/PEGDMA material was much higher than that of the neat matrix, as shown in Figure 12. This behavior is ascribed to the softening effect produced by the partial melting of the supramolecular network at 80 °C. As expected, when shape memory cycles were performed setting 30 °C as the T_{high}, both the BCP/PEGDMA material and the neat matrix exhibited very similar behaviors (Figure S11). Considering these results, it is possible to conclude that programming the T_{high} within the melting range of the supramolecular network can be used as a versatile way to tune the maximum strain of these materials.

CONCLUSIONS

We have studied the behavior of supramolecular networks obtained by CDSA of PE-*b*-PEO in a dimethacrylate matrix. The supramolecular structure is formed by lamellar aggregates of nanoribbons that are interconnected through crystalline nodes. In turn, nanoribbons consist of a semicrystalline PE core bordered by coronal chains of PEO. The dimethacrylate matrix preserves the structure of the supramolecular network and avoids its disintegration when the material is heated above the melting temperature of PE cores. Furthermore, the matrix does not influence the crystallization—melting processes of PE, which take place through the interconnected cores of the supramolecular network. In contrast, the matrix imposes strong effects of topological confinement on the crystallization of PEO, limiting the dimensions of the crystalline lamellae that can be formed. The maximum strain of these materials can be precisely tuned by programming the temperature within the melting range of the supramolecular network.

ASSOCIATED CONTENT

ⓢ Supporting Information

The Supporting Information is available free of charge at https://pubs.acs.org/doi/10.1021/acs.macromol.2c02218.

> Gelation process followed by optical microscopy in real time; PLOM images at room temperature of PE-*b*-PEO/PEGDMA blends containing 10 and 20 wt % PE-*b*-PEO; DSC scans for a non-photopolymerized blend containing 30 wt % PE-*b*-PEO in a PEGDMA monomer; conversion of methacrylate groups as a function of irradiation time; fitting parameters of SAXS data and description of the models used; DSC scans for photocured materials containing 20, 10, and 5 wt % PE-*b*-PEO; PLOM images acquired during heating—cooling cycles for a photopolymerized sample and a non-photopolymerized sample, both containing 10 wt % PE-*b*-PEO in PEGDMA; Avrami analysis for photocured samples containing 10, 20, and 30 wt % PE-*b*-PEO in PEGDMA; cooling and heating DSC scans after SN at different T_s values for photocured materials containing 20, 10, and 5 wt % PE-*b*-PEO; and strain-recovery cyclic tests under controlled force mode setting T_{high} = 30 °C (PDF)
>
> Video of the gelation process followed by optical microscopy in real time (AVI)

AUTHOR INFORMATION

Corresponding Authors

Alejandro J. Müller − POLYMAT and Department of Polymers and Advanced Materials: Physics, Chemistry and Technology, Faculty of Chemistry, University of the Basque Country UPV/EHU, 20018 Donostia-San Sebastián, Spain; IKERBASQUE, Basque Foundation for Science, Bilbao 48009, Spain; ⓞ orcid.org/0000-0001-7009-7715; Email: alejandrojesus.muller@ehu.es

Walter F. Schroeder − Institute of Materials Science and Technology (INTEMA), University of Mar del Plata and National Research Council (CONICET), 7600 Mar del Plata, Argentina; ⓞ orcid.org/0000-0002-0232-4282; Email: wschroeder@fi.mdp.edu.ar

Authors

Ruth N. Schmarsow − Institute of Materials Science and Technology (INTEMA), University of Mar del Plata and National Research Council (CONICET), 7600 Mar del Plata, Argentina

Ulises Casado − Institute of Materials Science and Technology (INTEMA), University of Mar del Plata and National Research Council (CONICET), 7600 Mar del Plata, Argentina

Marcelo Ceolín − Instituto de Investigaciones Fisicoquímicas Teóricas y Aplicadas (INIFTA), Universidad Nacional de La Plata, CONICET, 1900 La Plata, Argentina

Ileana A. Zucchi − Institute of Materials Science and Technology (INTEMA), University of Mar del Plata and National Research Council (CONICET), 7600 Mar del Plata, Argentina

Complete contact information is available at:
https://pubs.acs.org/10.1021/acs.macromol.2c02218

Author Contributions

The manuscript was written through contributions of all authors. All authors have given approval to the final version of the manuscript.

Notes

The authors declare no competing financial interest.

ACKNOWLEDGMENTS

REFERENCES

(1) Lugger, S. J. D.; Houben, S. J. A.; Foelen, Y.; Debije, M. G.; Schenning, A. P. H. J.; Mulder, D. J. Hydrogen-Bonded Supramolecular Liquid Crystal Polymers: Smart Materials with Stimuli-Responsive, Self-Healing, and Recyclable Properties. *Chem. Rev.* **2022**, *122*, 4946−4975.

(2) Wu, C.; Huang, J.; Chu, B.; Deng, J.; Zhang, Z.; Tang, S.; Wang, X.; Wang, Z.; Wang, Y. Dynamic and Hierarchically Structured Networks with Tissue-like Mechanical Behavior. *ACS Nano* **2019**, *13*, 10727−10736.

(3) Panja, S.; Adams, D. J. Stimuli Responsive Dynamic Transformations in Supramolecular Gels. *Chem. Soc. Rev.* **2021**, *50*, 5165−5200.

(4) Chivers, P. R. A.; Smith, D. K. Shaping and Structuring Supramolecular Gels. *Nat. Rev. Mater.* **2019**, *4*, 463−478.

(5) Yan, H.; Qiu, Y.; Wang, J.; Jiang, Q.; Wang, H.; Liao, Y.; Xie, X. Wholly Visible-Light-Responsive Host-Guest Supramolecular Gels

Based on Methoxy Azobenzene and β-Cyclodextrin Dimers. *Langmuir* **2020**, *36*, 7408−7417.

(6) Xian, S.; Webber, M. J. Temperature-Responsive Supramolecular Hydrogels. *J. Mater. Chem. B* **2020**, *8*, 9197−9211.

(7) Núñez-Villanueva, D.; Jinks, M. A.; Gómez Magenti, J.; Hunter, C. A. Ultrasound-Induced Gelation of a Giant Macrocycle. *Chem. Commun.* **2018**, *54*, 10874−10877.

(8) Zhang, S.; Bellinger, A. M.; Glettig, D. L.; Barman, R.; Lee, Y. A. L.; Zhu, J.; Cleveland, C.; Montgomery, V. A.; Gu, L.; Nash, L. D.; Maitland, D. J. A pH-Responsive Supramolecular Polymer Gel as an Enteric Elastomer for Use in Gastric Devices. *Nat. Mater.* **2015**, *14*, 1065−1071.

(9) Ji, W.; Yuan, C.; Chakraborty, P.; Makam, P.; Bera, S.; Rencus-Lazar, S.; Li, J.; Yan, X.; Gazit, E. Coassembly-Induced Transformation of Dipeptide Amyloid-Like Structures into Stimuli-Responsive Supramolecular Materials. *ACS Nano* **2020**, *14*, 7181−7190.

(10) Jiao, T., Ed. *Supramolecular Gels: Materials and Emerging Applications*; Weinheim: Germany, 2021.

(11) Wang, X. S.; Guerin, G.; Wang, H.; Wang, Y.; Manners, I.; Winnik, M. A. Cylindrical Block Copolymer Micelles and Co-Micelles of Controlled Length and Architecture. *Science* **2007**, *317*, 644−647.

(12) Gädt, T.; Ieong, N. S.; Cambridge, G.; Winnik, M. A.; Manners, I. Complex and Hierarchical Micelle Architectures from Diblock Copolymers using Living Crystallization-Driven Polymerizations. *Nat. Mater.* **2009**, *8*, 144−150.

(13) Schmelz, J.; Karg, M.; Hellweg, T.; Schmalz, H. General Pathway toward Crystalline-Core Micelles with Tunable Morphology and Corona Segregation. *ACS Nano* **2011**, *5*, 9523−9534.

(14) Zucchi, I. A.; Schroeder, W. F. Nanoribbons with Semicrystalline Core Dispersed in a Visible-Light Photopolymerized Epoxy Network. *Polymer* **2015**, *56*, 300−308.

(15) Song, S.; Liu, X.; Nikbin, E.; Howe, J. Y.; Yu, Q.; Manners, I.; Winnik, M. A. Uniform 1D Micelles and Patchy Block Comicelles via Scalable, One-Step Crystallization-Driven Block Copolymer Self-Assembly. *J. Am. Chem. Soc.* **2021**, *143*, 6266−6280.

(16) Du, Z. X.; Xu, J. T.; Fan, Z. Q. Micellar Morphologies of Poly(ε-caprolactone)-*b*-poly(ethylene oxide) Block Copolymers in Water with a Crystalline Core. *Macromolecules* **2007**, *40*, 7633−7637.

(17) Bang, J.; Jeong, U.; Ryu, D. Y.; Russell, T. P.; Hawker, C. J. Block Copolymer Nanolithography: Translation of Molecular Level Control to Nanoscale Patterns. *Adv. Mater.* **2009**, *21*, 4769−4792.

(18) Garcia-Hernandez, J. D.; Kang, Y.; Fukui, T.; Finnegan, J. R.; Manners, I. Fiberlike Micelle Networks from the Solution Self-Assembly of B-A-B Triblock Copolymers with Crystallizable Terminal Polycarbonate Segments. *Macromolecules* **2022**, *55*, 3821−3830.

(19) Gankema, H.; Hempenius, M. A.; Möller, M.; Johansson, G.; Percec, V. Gel Template Leaching an Approach to Functional Nanoporous Membranes. *Macromol. Symp.* **1996**, *102*, 381−390.

(20) Stendahl, J. C.; Li, L.; Zubarev, E. R.; Chen, Y. R.; Stupp, S. I. Toughening of Polymers by Self-Assembling Molecules. *Adv. Mater.* **2002**, *14*, 1540−1543.

(21) Chen, J.; Liu, J.; Thundat, T.; Zeng, H. Polypyrrole-Doped Conductive Supramolecular Elastomer with Stretchability, Rapid Self-Healing, and Adhesive Property for Flexible Electronic Sensors. *ACS Appl. Mater. Interfaces* **2019**, *11*, 18720−18729.

(22) Li, C. H.; Zuo, J. L. Self-Healing Polymers Based on Coordination Bonds. *Adv. Mater.* **2020**, *32*, No. 1903762.

(23) Guo, Q.; Zhang, X.; Zhao, F.; Song, Q.; Su, G.; Tan, Y.; Tao, Q.; Zhou, T.; Yu, Y.; Zhou, Z.; Lu, C. Protein-Inspired Self-Healable Ti₃C₂ MXenes/Rubber-Based Supramolecular Elastomer for Intelligent Sensing. *ACS Nano* **2020**, *14*, 2788−2797.

(24) Rossow, T.; Hackelbusch, S.; van Assenbergh, P.; Seiffert, S. A Modular Construction Kit for Supramolecular Polymer Gels. *Polym. Chem.* **2013**, *4*, 2515−2527.

(25) Liu, Y.; Cai, L.; Ma, L.; Li, M.; Yang, J.; Chen, K.; Yin, P. Modulating Polymer Dynamics via Supramolecular Interaction with Ultrasmall Nanocages for Recyclable Gas Separation Membranes with Intrinsic Microporosity. *Nano Lett.* **2021**, *21*, 9021−9029.

(26) Balsamo, V.; Urdaneta, N.; Pérez, L.; Carrizales, P.; Abetz, V.; Müller, A. J. Effect of the Polyethylene Confinement and Topology on its Crystallization within Semicrystalline ABC Triblock Copolymers. *Eur. Polym. J.* **2004**, *40*, 1033−1049.

(27) Müller, A. J.; Balsamo, V.; Arnal, M. L. Nucleation and Crystallization in Diblock and Triblock Copolymers. *Adv. Polym. Sci.* **2005**, *190*, 1−63.

(28) Fillon, B.; Wittmann, J.; Lotz, B.; Thierry, A. Self-Nucleation and Recrystallization of Isotactic Polypropylene (α Phase) Investigated by Differential Scanning Calorimetry. *J. Polym. Sci., Part B: Polym. Phys.* **1993**, *31*, 1383−1393.

(29) Michell, R. M.; Mugica, A.; Zubitur, M.; Müller, A. J. Self-Nucleation of Crystalline Phases Within Homopolymers, Polymer Blends, Copolymers, and Nanocomposites. In *Polymer Crystallization I*; Advances in Polymer Science; Springer: Cham, 2017; vol. *276*, pp. 215−256.

(30) Sangroniz, L.; Cavallo, D.; Müller, A. J. Self-Nucleation Effects on Polymer Crystallization. *Macromolecules* **2020**, *53*, 4581−4604.

(31) Müller, A. J.; Hernández, Z. H.; Arnal, M. L.; Sánchez, J. J. Successive Self-Nucleation/Annealing (SSA): A Novel Technique to Study Molecular Segregation During Crystallization. *Polym. Bull.* **1997**, *39*, 465−472.

(32) Müller, A. J.; Michell, R. M.; Pérez, R. A.; Lorenzo, A. T. Successive Self-Nucleation and Annealing (SSA): Correct Design of Thermal Protocol and Applications. *Eur. Polym. J.* **2015**, *65*, 132−154.

(33) Pérez-Camargo, R. A.; Cavallo, D.; Müller, A. J. Recent Applications of the Successive Self-Nucleation and Annealing Thermal Fractionation Technique. *Front. Soft Matter* **2022**, *2*, No. 1003500.

(34) Breßler, I.; Kohlbrecher, J.; Thünemann, A. F. SASfit: A Tool for Small-Angle Scattering Data Analysis Using a Library of Analytical Expressions. *J. Appl. Crystallogr.* **2015**, *48*, 1587−1598.

(35) Glatter, O. *Scattering Methods and their Application in Colloid and Interface Science*; Elsevier, 2018.

(36) Schmarsow, R. N.; Ceolín, M.; Zucchi, I. A.; Schroeder, W. F. Core-Crystalline Nanoribbons of Controlled Length via Diffusion-Limited Colloid Aggregation. *Soft Matter* **2019**, *15*, 4751−4760.

(37) Castillo, R. V.; Arnal, M. L.; Müller, A. J.; Hamley, I. W.; Castelletto, V.; Schmalz, H.; Abetz, V. Fractionated Crystallization and Fractionated Melting of Confined PEO Microdomains in PB-*b*-PEO and PE-*b*-PEO Diblock Copolymers. *Macromolecules* **2008**, *41*, 879−889.

(38) Yin, J.; Raegen, A.; Idziak, S. H. J.; Forrest, J. A. Crystallization and Melting of Highly Monodisperse Poly(ethylene-oxide). *Soft Matter* **2020**, *16*, 7958−7969.

(39) Pfefferkorn, D.; Kyeremateng, S. O.; Busse, K.; Kammer, H. W.; Thurn-Albrecht, T.; Kressler, J. Crystallization and Melting of Poly(ethylene oxide) in Blends and Diblock Copolymers with Poly(methyl acrylate). *Macromolecules* **2011**, *44*, 2953−2963.

(40) Takahashi, Y.; Tadokoro, H. Structural Studies of Polyethers, (−(CH₂)m-O-)n. X. Crystal Structure of Poly(ethylene oxide). *Macromolecules* **1973**, *6*, 672−675.

(41) Buckley, C. P.; Kovacs, A. J. Melting Behaviour of Low Molecular Weight Poly(ethylene-oxide) Fractions. *Polym. Aspekte* **1975**, *58*, 44−52.

(42) Wong, R. S. H.; Ashton, M.; Dodou, K. Effect of Crosslinking Agent Concentration on the Properties of Unmedicated Hydrogels. *Pharmaceutics* **2015**, *7*, 305−319.

(43) Pielichowski, K.; Flejtuch, K. Differential Scanning Calorimetry Studies on Poly(ethylene glycol) with Different Molecular Weights for Thermal Energy Storage Materials. *Polym. Adv. Technol.* **2002**, *13*, 690−696.

(44) Lorenzo, A. T.; Arnal, M. L.; Albuerne, J.; Müller, A. J. DSC Isothermal Polymer Crystallization Kinetics Measurements and the Use of the Avrami Equation to Fit the Data: Guidelines to Avoid Common Problems. *Polym. Test.* **2007**, *26*, 222−231.

(45) Pérez-Camargo, R. A.; Liu, G.-M.; Wang, D.-J.; Müller, A. J. Experimental and Data Fitting Guidelines for the Determination of

Polymer Crystallization Kinetics. *Chin. J. Polym. Sci.* **2022**, *40*, 658−691.

(46) Michell, R. M.; Müller, A. J. Confined Crystallization of Polymeric Materials. *Prog. Polym. Sci.* **2016**, *54*, 183−213.

(47) Li, J. L.; Liu, X. Y. Architecture of Supramolecular Soft Functional Materials: From Understanding to Micro-/Nanoscale Engineering. *Adv. Funct. Mater.* **2010**, *20*, 3196−3216.

(48) Luo, X. F.; Mather, P. T. Preparation and Characterization of Shape Memory Elastomeric Composites. *Macromolecules* **2009**, *42*, 7251−7253.

📖 Recommended by ACS

Tuning the Plasticization to Decouple the Effect of Molecular Recoiling Stress from Modulus and Viscosity in Dewetting Thin Polystyrene Films

Mithun Madhusudanan, Mithun Chowdhury, *et al.*

FEBRUARY 09, 2023
MACROMOLECULES   READ 🗗

Poisoning by Purity: What Stops Stereocomplex Crystallization in Polylactide Racemate?

Jiaming Cui, Goran Ungar, *et al.*

JANUARY 21, 2023
MACROMOLECULES   READ 🗗

Tough Glass with Mechanical Bonding Network Anchored by High-Mobility Polymers

Kazuaki Kato, Kohzo Ito, *et al.*

MARCH 01, 2023
MACROMOLECULES   READ 🗗

Achieving High Permittivity Paraelectric Behavior in Mesogen-Free Sulfonylated Chiral Polyethers with Smectic C Liquid Crystalline Self-Assembly

Man-Hin Kwok, Lei Zhu, *et al.*

FEBRUARY 23, 2023
MACROMOLECULES   READ 🗗

Get More Suggestions >